# Characterizing Single Photon Emission From Quantum Dots in Nanowires

by

Morgan Mastrovich

A thesis
presented to the University of Waterloo
in fulfillment of the
thesis requirement for the degree of
Masters of Science
in
Physics (Quantum Information)

Waterloo, Ontario, Canada, 2019

# Author's Declaration

I hereby declare that I am the sole author of this thesis. This is a true copy of the thesis, including any required final revisions, as accepted by my examiners.

I understand that my thesis may be made electronically available to the public.

# Abstract

Bright sources of highly indistinguishable single photons are desirable for diverse applications in quantum technology, including quantum cryptographic protocols, information processing, and metrology. The most common single photon source for quantum optical experiments is currently spontaneous parametric downconversion (SPDC); quantum dot sources have the potential to greatly exceed the brightness of these current sources, without compromising the quality of the emitted photons. Embedding a quantum dot within a tapered nanowire waveguide greatly increases the photon extraction efficiency. Exciting a two-photon resonant transition decreases the emission time jitter, improving both the multi-photon suppression and indistinguishability. Before this work, these two techniques have not yet been implemented together.

We implemented two-photon resonant excitation (TPRE) for the first time in nanowire-embedded quantum dots; we found that it significantly improved the multi-photon suppression. However, we were unable to measure the indistinguishability due to low counts and instabilities in the experimental apparatus. Nevertheless, we have identified the significant improvements that are still required in order to successfully measure the indistinguishability under TPRE; with these improvements, the measurement should be possible for future group members. We successfully measured the indistinguishability under a quasi-resonant excitation, but did not find a significant difference when comparing to the measurement made on a similar quantum dot under above-bandgap excitation. We must also substantially improve the single photon count rate in order to approach the polarization entanglement rates of SPDC sources. Despite these challenges, nanowire-embedded quantum dots remain a promising source of both single and entangled pairs of photons.

# Acknowledgements

Many thanks to Dr. Kevin Resch and Dr. Michael Reimer, for providing an interesting project and scientific guidance. This thesis would not exist without your mentorship, feedback, and support.

Thank you to the Quantum Optics and Quantum Information group for being supportive colleagues, generous with your time and advice (and excellent coffee conversations!).

A big thanks to the Quantum Photonic Devices group for being my research family at RAC1! You were all so very welcoming and inclusive, unofficially adopting me into your group. You made me feel at home and part of the team, and made my time at RAC1 truly enjoyable.

A special thanks to Arash Ahmadi for being a wonderful collaborator and lab buddy. It was a true pleasure to work in the lab alongside a fellow researcher who is also a great friend, one who values my humanity and emotional wellbeing before my scientific productivity.

Many thanks as well to Klaus Jöns, for your unparalleled TPRE expertise, unflagging and inspiring work ethic, and excellent mentorship.

It takes a village to write a thesis! Several wonderful people deserve a generous heap of thanks, Eduardo Martín Martinez, Júlia Amoros Binefa, and Simon Daley, who gave generously of their time and read many drafts of this thesis. I appreciate your constructive criticism and insightful suggestions.

I am incredibly lucky to be surrounded by many excellent humans, folks who have made my life more rich and wonderful by crossing my path; I am so very thankful to be part of such an interconnected and caring community! There are a few folks who have been a special presence in my life, providing companionship, support, and sustenance, and to whom I owe an extra mention.

To Phillip Diffley, for giving me a nudge in the right direction when I needed it most.

To my Hickory family, Kayla, Romain, Vic, and Chester: you have made Waterloo truly home, and I am so thankful to share space, food, laughter, and many warm memories

with you! Thank you for making Waterloo a brighter place, and for making this run-down student house a home!

To my parents, Valerie and Charlie, to my sister Sydney, and to my dear friends, Melissa Galonsky, Chloé Calvarin, Miranda Thompson, Eduardo Martín Martinez, Cliff Plesha, Stefanie Beale, Simon Daley, Kayla Hardie, Júlia Amoros Binefa, and Thendral Govindaraj: Writing this thesis would not have been possible without your support. For your patience, your empathy, your overflowing kindness and bottomless love, I will be forever grateful.

# Dedication

*To my mother, Valerie* ~

You showed me the strength and taught me all the skills I needed
to weather the biggest challenge of my life,
and emerge more whole.

For this, and for your generous and nurturing love, I am forever in your debt.

# Table of Contents

# List of Figures

# List of Tables

# Chapter 1

# Introduction

Single photon sources are useful for a variety of technological applications. Many prominent protocols implementing quantum key distribution — a method of producing a secret cryptographic key securely shared between two parties — require a stable and predictable single photon source. The precision of metrological tasks such as positioning and clock-synchronization can be significantly improved by using high quality single photon sources. Additionally, single photon sources are also used in a proposed redefinition of the candela, the SI base unit for luminous intensity. Finally, single photon sources can be used to make a probabilistic source of polarization-entangled states, which are extremely useful for implementing quantum state teleportation protocols and building quantum repeaters.

Thus, a device with the ability to produce a single quantum of light in a repeatable fashion is highly sought-after. Recent improvement in the quality of such devices has been promising. Though many physical systems — including atoms, ions, non-linear crystals, diamond, and semiconductor nanostructures such as quantum dots — can produce quantum states of light. The ideal single photon source has not yet been created, despite impressive technological development in the control and manipulation of many of these quantum systems. Several research groups have begun to commercialize the quantum dot-based single photon sources developed in their labs, suggesting that significant demand for high quality single photon sources is anticipated.

Single photon autocorrelation and indistinguishability are the most important characteristics for assessing the quality of single photon sources, as they are required for all applications. In this thesis, I present measurements of the single photon autocorrelation and indistinguishability of the emissions from a quantum dot in a tapered nanowire excited in several different ways.

This chapter will provide an introduction to single photon sources and their applications.

The first section of this chapter presents the field consensus of what constitutes an ideal single photon source. The next section briefly introduces the measurements necessary to characterize two of the most important single photon source properties. The final two sections give a brief overview of the most relevant applications of single photon sources: in quantum communication technology and quantum metrology, and as essential constituents of a source of polarization-entangled photons.

## 1.1 Ideal single photon source

The essential qualities of an ideal single photon source are [15]:

1. **Bright**, emitting many photons per unit time.
2. **On-demand**, emitting a photon when stimulated.
3. **High single photon autocorrelation**, emitting only one photon at a time.
4. **High indistinguishability**, emitting photons that are identical in all characteristics.

These qualities are necessary for every application, and are considered important for measuring progress in single photon source design.

## 1.2 Applications: communication and metrology

Photons are not ideal candidates for quantum computation because they do not interact with each other; however, photons are an excellent medium for encoding and sending information over long distances. Over the past few decades, quantum communication technology has been industriously developed, predominantly quantum key distribution (QKD). In this family of cryptographic schemes, a sender encodes a string of bits (the secret key) in a sequence of photons, sends that sequence to a partner, and publicly shares the encoding basis for each photon. Their accomplice can then decode the secret key by measuring each of the received photons in the correct basis, while at the same time certifying with exponentially increasing certainty that no eavesdropper has intercepted the message. 'Prepare-and-measure' protocols such as BB84, the first QKD protocol, require a stream of single photons in order to transmit the secret key with complete security, relying on the single photon purity of the light, the no-cloning theorem, and the effect of measurement on quantum systems in order to detect the presence of an eavesdropper.

QKD has been implemented successfully using an attenuated laser as a photon source by using the decoy state protocol; however, this protocol requires exponentially increasing resources in order to guarantee security.

Even though QKD protocols are still under active development, practical implementations have already found their way into a variety of applications, from finance to telecommunications, to experiments in low-Earth orbit. For a decade, Swiss banks have been encoding sensitive transactions using QKD systems produced by ID Quantique. More recently, China launched the satellite Micius, equipped to send single photon pulses and test QKD protocols from space.

Single photons also have the potential to improve several areas of metrology, including the quantum-positioning and clock-synchronization protocol [6]. A redefinition of the candela [3], the SI base unit of luminous intensity, proposes measuring a countable number of single photons instead of the power of a thermal source. Depending on the quality of the single photon source and the timing resolution of the detectors, this quantum definition could dramatically improve the precision of the candela and all SI units derived from it [3].

## 1.3 Postselected entanglement

Another use for a bright, efficient single photon source is in the production of polarization-entangled states [15] through a probabilistic scheme involving overlap at a beamsplitter and temporal postselection. This scheme has the potential to be an excellent source of entangled photons, as long as the single photon source is bright and the transmission efficiency of the setup is close to unity.

Entanglement is an inextricable feature of quantum mechanics. A fundamentally multi-particle state that cannot be factored has some degree of entanglement [11]:

$$\hat{\rho}_{AB} \neq \sum_i p_i \, \hat{\rho}_A \otimes \hat{\rho}_B, \tag{1.1}$$

with $p_i \in [0,1]$ and $\sum_i p_i = 1$. In an entangled state such as equation 1.1, there exist correlations between subsystems A and B that cannot be explained classically [**?** ]. As a concrete example, consider a particle that has two possible spin states, up ($|\uparrow\rangle$) and down ($|\downarrow\rangle$). A bipartite system of two such particles could be prepared in the state

$$|\Psi^-\rangle = \frac{1}{\sqrt{2}} \left( |\uparrow_A \downarrow_B\rangle - |\downarrow_A \uparrow_B\rangle \right). \tag{1.2}$$

This is an example of a Bell State, a class of maximally entangled bipartite states for two-dimensional quantum systems [11].

Notice that the measured spin state of each particle in equation 1.2 is not predetermined. Notice that this is also true for a classical ensemble with statistical uncertainty, such as the mixed state

$$\hat{\rho} = \frac{1}{2}\Big( |\uparrow_A \downarrow_B\rangle \langle \uparrow_A \downarrow_B| + |\downarrow_A \uparrow_B\rangle \langle \downarrow_A \uparrow_B| \Big). \tag{1.3}$$

However, for the maximally entangled state $|\Psi^-\rangle$, the outcomes of local measurements on subsystems A and B are completely probabilistic, but the correlations between measurements of those subsystems are fully determined by the joint state. The outcome of measuring the spin of particle A is fully correlated with the outcome of a spin measurement on particle B, regardless of the measurement outcome. That is the essence of entanglement; the correlations in both phase and measurement outcome make maximally entangled states like equation 1.2 special.

Entangled states are crucial resources for communication schemes that utilize quantum resources to provide speed-ups and security boosts. A majority of existing quantum communication protocols require a high quality source of entangled photons to gain an advantage over existing technologies. Additionally, accurate measurements in the Bell state basis are necessary for most major types of quantum communication, including quantum repeaters and quantum state teleportation. These measurements project a state onto the two-dimensional space of Bell states, and require interference on a beamsplitter. This measurement can only be realized with high fidelity if the incident photons are completely indistinguishable in all degrees of freedom, except that which is used to encode the Bell state (often polarization). Consequently, each of the individual photons in an ideal polarization-entangled state must also have all of the properties required of an ideal single photon source (listed in Section 1.1). Thus, the ability to produce a stream of indistinguishable single photons at regular intervals is crucial to many methods of producing entangled photon states.

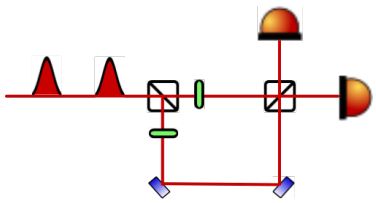

Figure 1.1: Unbalanced Mach-Zender interferometer to produce 2-photon entanglement (delay length not to scale).

A bright source of indistinguishable single photons can be used to create both entangled pairs and triplets through a straightforward scheme using an unbalanced Mach-Zender interferometer and coincidence postselection, shown in figure 1.1. To form a two-photon

entangled state, a photon is sent down a delay path by a polarizing beamsplitter (PBS 1), which delays the photon by exactly the distance between subsequent photons. It is then overlapped with the subsequent photon at the second polarizing beamsplitter (PBS 2). Both photons are made to be diagonally polarized before arriving at PBS 2; thus, there are four possible ways for these photons to exit that beamsplitter. We postselect on coincidences, ensuring that we only measure states that exit the beamsplitter from opposite ports and are either both $|H\rangle$ or $|V\rangle$. If the photons are indistinguishable, the detected state will be entangled in polarization. Entangled triplets can be produced by a straightforward extension of the pairs scheme, shown in Figure 1.2. A second delay, twice as long as the first, is added, also in free space and using polarizing beamsplitters. Entanglement can be verified by measuring correlationsin three orthogonal polarization bases, as proposed in James et. al. [**?** ]

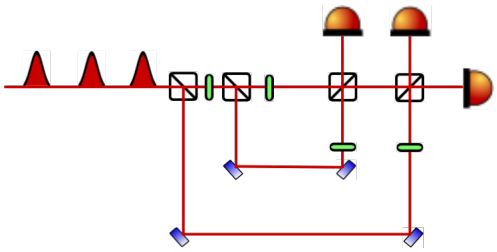

Figure 1.2: Unbalanced Mach-Zender interferometer with two delay arms to produce 3-photon polarization-entangled states.

To evaluate the potential of this scheme, we compare the predicted rates we predict with established sources of polarization entanglement. Spontaneous parametric downconversion (SPDC) is a nonlinear process that converts one photon to two, while conserving energy and momentum [10]. It has been harnessed for the past several decades to produce polarization entangled photon pairs using a variety of experimental configurations, each producing entangled states at different rates. An early implementation by Kwiat et. al. in 1995 yielded entangled pairs at a rate of 1.5 kHz [10]; this rate was improved significantly over the next decade to 1.2 MHz [1]. SPDC has also been used to create entangled triplet sources in two different configurations: a cascaded downconversion scheme produced triplets at 0.19 Hz [7], while a more efficient postselection scheme yielded 39 Hz [4].

The postselected schemes described above (and shown in Figure 1.1) have the potential to far exceed the highest rates achieved by SPDC-based sources to date, if the brightness of the single photon source and efficiency of the collection and detection is high. We have previously measured a single photon count rate of 1 MHz under 76 MHz excitation. After doubling the repetition rate, we will have a single photon count rate of 2 MHz, but the

probability of getting a photon in each pulse still remains $P = \frac{1}{76}$. We use this probability to calculate the entanglement rates that we can expect from this source. Assuming that our collection set-up compensates for polarization rotations, we expect half of photons incident on the first PBS to take each path. The probability of two subsequent photons being emitted and successfully detected is $P^2$. There is a $\frac{1}{4}$ probability that those photons take the appropriate paths to arrive simultaneously at the recombining beamsplitter, and a $\frac{1}{2}$ probability that the photons antibunch at that beamsplitter, creating a coincidence count. We therefore expect our source to yield two-photon entanglement at a rate of 3.29 kHz.

By extension, to obtain three-photon entanglement, three subsequent photons must be produced by the dot (with probability $P^3$). These photons must take, respectively, the long delay path (with probability $\frac{1}{2}$), short delay path (with probability $\frac{1}{4}$), and the direct path (with probability $\frac{1}{4}$). Thus, there is a $\frac{1}{32}$ probability of three photons arriving simultaneously to the recombining beamsplitters, and a $\frac{1}{4}$ probability of all three photons antibunching. Combining these probabilities, there is a $\frac{1}{128}$ probability of registering a 3-fold coincidence. Thus, we expect our single photon source to produce three-photon entanglement at a rate of 2.7 Hz.

At first glance, one may think that this scheme scales well to entangled states with more photons. However, scaling to larger states is actually quite impractical, as the table space required for delay paths is exorbitant, and the generation rate of $n$-photon states scales exponentially with increasing $n$. At our current single count rates, we cannot produce entangled pairs or triplets at a rate even remotely comparable to the best SPDC entanglement sources [1, 4]. We must significantly increase the single photon count rate in order to successfully surpass cutting-edge entanglement sources. Despite the discouraging prospects, this scheme for postselected entanglement is still interesting to pursue as a proof of principle for small entangled states, because it shows promise of beating the best rates of polarization entanglement generation. Additionally, this scheme could be miniaturized onto a chip, which would eliminate both alignment difficulties and stability concerns. This has potential to be a readily implementable source of polarization entangled states of three or more indistinguishable photons.

# Chapter 2

# Quantum Dot Background

A quantum dot is a nanoscale semiconductor structure designed to confine charge carriers in a way that allows radiative recombination and maximizes single photon emission. While confined within the quantum dot, these charge carriers have discrete energy states bundled into shells, much like the energy levels of electrons in an atom. The depth of the confining potential, along with the quantum dot shape and size, determines the spacing of energy levels, which in turn determines the energy of the emitted photons. For most types of quantum dots, the energy of these transitions is conveniently in the visible, near-infrared, or telecom spectra, and are addressable with light sources that are already well-developed, thoroughly studied, and easy to obtain; efficient fiber and optical components have also been developed at most of these wavelengths. Thus, quantum dots are a promising source of single photons for telecom and quantum communication applications and for laboratory use.

In this chapter, I provide an overview of the knowledge of quantum dots required to understand the context for the research presented in this thesis. In the first two sections, I give a brief summary of how quantum dots are designed to produce single photons and engineered to optimize the properties of these photons. Then, in the third section, I contrast several methods of exciting the quantum dot, and explore the effect of the excitation type on the properties of the emitted photons. In the final section, I delve a bit into the mathematics of resonant excitation, in order to explain Rabi oscillations, a signature of resonance.

## 2.1 Quantum Dot Structure and Function

A quantum dot is a three-dimensional semiconductor heterostructure composed of two juxtaposed heterojunctions in each dimension. Each of these heterojunctions must have a band alignment that is capable of trapping both electrons in the conduction band, and holes — the quasiparticles that form when an electron is excited and leaves behind a net positive charge — in the valence band.

A heterojunction is simply an interface of two semiconductors with different band gaps, exploiting the difference between the semiconductor potentials to manipulate the spatial location of charge carriers. It is not just the relative band gap energies that determine the heterojunction properties — the alignment of the valence and conduction band edges also plays a crucial role in charge carrier confinement. In general, there are three ways that the valence and conduction bands of semiconductors in a heterojunction can be aligned, as illustrated in Figure 2.1 [14]:

1. **Type I**, where electrons and holes are trapped in the same material layer.
2. **Type II**, staggered band alignment, where electrons and holes are trapped in different material layers, and thus spatially separated.
3. **Type III**, broken band alignment, where charge carriers are not trapped at all. Instead, electrons flow from the valence band of one material to the conduction band of the other, while holes flow in the opposite direction.

This alignment determines the location and strength of the confinement of charge carriers.

A device that can successfully trap both electrons and holes can be produced by placing two Type I heterojunctions next to one another, so that a material with a smaller bandgap is sandwiched between another material with a larger band gap. To trap electrons, the conduction band of the outer material must have a higher energy than that of the inner material. Conversely, to trap holes, the valence band of the inner material must be higher energy than that of the outer material (because of the opposite charge of holes). Thus, to be considered a quantum dot, a heterostructure must have two juxtaposed both heterojunctions in a quantum dot must have Type I band alignment in all three dimensions.

In general, the confining potential of a quantum dot is influenced by many factors: band gap and alignment, dot shape and size, and the electric fields in the dot vicinity. It is most thorough to calculate this potential and the resulting energy levels with an atomistic approach [], but, as in Perinetti [**?** ], we take a more simple approach, as these calculations

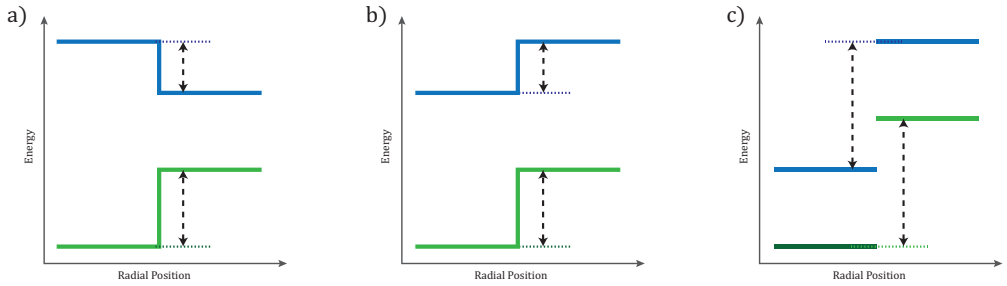


Figure 2.1: Band diagrams of three common types of semiconductor heterojunction [14]: a) Type I, b) Type II, and c) Type III. The conduction band is drawn in blue, and the valence band in green; the trapping potentials for both electrons and holes are denoted with dashed arrows.

are not the focus of this thesis. The confining potential of a quantum dot in a nanowire can be modeled in the growth direction (the direction of photon propagation) as a finite square well potential; the lateral potential is well-approximated by a harmonic oscillator, illustrated in figure 2.2. Solving the harmonic potential for the radial quantization, energy levels are obtained that can be labeled by the quantum numbers for energy, $n$, and total angular momentum, $\ell$. The energy of each state is [**?** ]

$$E(n,\ell) = \left(2n + |\ell| + 1\right)\,\hbar\omega_e, \tag{2.1}$$

where $\omega_e$ is the angular frequency of the electron. In analogy to atomic naming conventions, it is common practice to group together energy levels that are degenerate in the absence of strain and external fields: the lowest energy s-shell contains only the $(0,0)$ state; the p-shell, with an energy of $2\hbar\omega_e$, contains two states, $\{\,(0,\pm 1)\}$; the d-shell contains three states, $\{(2,0),(1,\pm 1)\}$. Limited in their capacity by the Pauli exclusion principle, these shells contain two, four, and six charge carriers, respectively. In this thesis, we work exclusively with photons produced by electrons and holes in the s-shell, occupying the lowest energy states of the quantum dot.

The quantum dot traps electrons and holes in the same material layer, confining the charge carriers with enough spatial overlap to form a bound state — a quasi-particle called an exciton. The energy of a single exciton trapped in the s-shell of a quantum dot (referred to as the "exciton state" and abbreviated throughout this thesis as X) is the sum of the energies of the electron and hole less the potential of their coulomb attraction:

$$E_X = E_e + E_h - V_{eh} \tag{2.2}$$

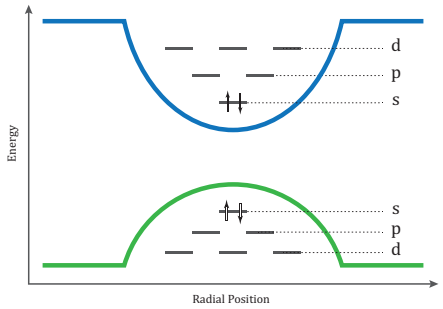


Figure 2.2: Potential energy schematic, showing shells s, p, and d, of electrons and holes (occupying, respectively, the conduction and valence bands) [14].

Similarly, two excitons occupying the the s-shell are collectively called the biexciton state (abbreviated throughout this thesis as XX). The energy of that state is the sum of its four constituent charge carriers and binding energy — the pairwise coulomb interactions between those particles:

$$E_{XX} = 2\,E_e + 2\,E_h - 4\,V_{eh} + V_{ee} + V_{hh}, \tag{2.3}$$

which simplifies to:

$$E_{XX} = 2\,E_X - 2\,V_{eh} + V_{ee} + V_{hh}. \tag{2.4}$$

When one of these excitons recombines, the state of the charge carriers confined in the quantum dot transitions from the XX to the X state. The energy of the emitted photon (labeled $\gamma_{XX}$ in figure 2.3) is the difference between the starting (XX) and ending (X) states. Similarly, when the remaining exciton recombines, the energy of the emitted photon ($\gamma_X$) is equal to the energy of the exciton state. From Equation 2.4, we can deduce that the energy of the biexciton state will be less than twice that of the exciton state, as long as the condition

$$2\,V_{eh} > V_{ee} + V_{hh} \tag{2.5}$$

is fulfilled. The depth of the confining potential of the quantum dot, which depends on the material properties and dot shape, determines the strength of the coulomb interaction. In our quantum dot, equation 2.5 is upheld, and the XX photon will be lower in energy than the X photon, $E_{\gamma XX} < E_{\gamma X}$.

The mechanics of single photon creation from a quantum dot using optical excitation can be summarized in three processes:

1. **Excitation**, in which the dot or surrounding material absorbs the incoming light pulse, exciting charge carriers.

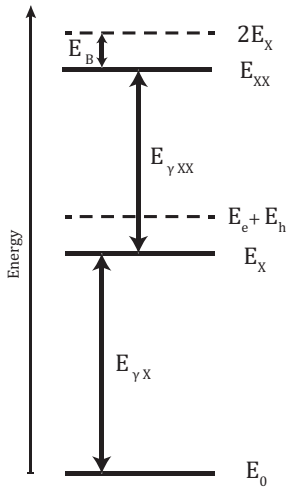


Figure 2.3: Energy diagram of charge carriers in various bound state configurations. The exciton and biexciton state energies are labeled as $E_{XX}$ and $E_X$, the ground state energy as $E_0$; the emitted photon energies $E_{\gamma XX}$ and $E_{\gamma X}$ and binding energy $E_B$ are denoted with vertical arrows; to guide the eye in comparing, the sum of the electron and hole energy $(E_e + E_h)$ and twice the exciton energy $(2E_X)$ are marked by a dotted line.

2. **Trapping**, in which the excited charge carriers are confined and occupy an energy level within the potential well.

3. **Recombination**, in which the excited electron decays, the quasi-particle recombines, and a photon is emitted.

Under the right conditions, a quantum dot can produce entangled photon pairs. Consider two excitons occupying the lowest energy level of the quantum well. These excitons recombine one after the other, emitting first the XX photon, then the X photon, as shown in figure 2.4. As discussed earlier in this section and illustrated in figure 2.3, the presence of a second exciton trapped in the dot changes the exciton energy; the X and XX photons are emitted at slightly different wavelengths, and they are entangled in polarization. When simultaneously occupying the s-shell, the two excitons must have opposite spins. One of the excitons must decay before the other, and thus the biexciton photon, $\gamma_{XX}$, will have two possible polarizations, $|R\rangle$ or $|L\rangle$, depending on the spin of the recombining exciton. The X photon will have the orthogonal circular polarization, either $|L\rangle$ or $|R\rangle$, since the remaining exciton must have an opposite spin to the one that decayed first. The spins of the two excitons are correlated, but the spin of the exciton that decays first will be

random. As long as $\gamma_X$ and $\gamma_{SXX}$ are indistinguishable, the photons will be entangled in polarization.

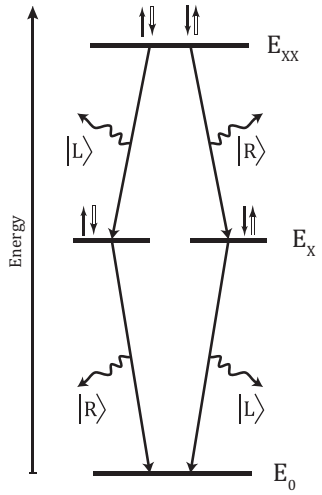


Figure 2.4: Energy level diagram illustrating the biexciton-exciton cascade: two excitons radiatively recombine in succession, emitting two photons that are polarization entangled.

## 2.2 Quantum Dot Devices

Quantum dots can be fabricated in a wide variety of ways, and embedded in a variety of nanostructures that improve different characteristics of the photon emission. Dots fabricated with Stranski-Krastanov growth are the most straightforward to fabricate, but suffer from low extraction efficiency. There are several dominant strategies for boosting the extraction efficiency: growing a reflective layer below the growth substrate that acts as a mirror, or embedding the quantum dot in a nanostructure, predominantly either a nanowire or microcavity. The nanowire acts as a broadband waveguide, increasing the emission into the guided mode, while the microcavity increases the emission rate of the quantum dot through the Purcell Effect.

It is also advantageous to attach electrodes to the nanostructure, in order to apply a transverse electric field to the dot. Alternatively, piezoelectric segments can be used to apply multi-axial strain in the transverse plane. Both techniques allow the experimenters to apply a unique electric or strain field to each dot, in order to cancel the fine structure splitting between the two exciton spin states and improve the entanglement properties.

Our device is an indium phosphide (InP) nanowire, tapered on one end, with a cylindrical region of indium arsenic phosphide (InAsP) embedded in the center, as seen in Figure ??. The nanowire is grown with a two-step process, using a combination of site-selective epitaxy and VLS chemical beam epitaxy. If the right growth rate and conditions are used, the waveguide will be pure wurtzite with no stacking faults. First, a grid of gold particles is deposited, the nanowire is grown vertically underneath the gold for 1 $\mu$m, and then arsine gas is added to form the quantum dot. After the arsine gas is removed, growth is continued to finish the core, allowing the Indium to diffuse up the wire. The epitaxy is switched to VLS, allowing a layer of InP to grow vertically from the substrate, forming the cladding. Finally, the growth conditions are altered to grow in a combination of these two types of growth to form the taper.

This bottom-up method for fabricating a quantum dot in a nanowire has several advantages. The pure wurtzite crystal growth minimizes stacking faults, keeping the spectral linewidth small. The tapered end of the nanowire minimizes the reflection loss as the emitted photons transition from propagating through the waveguide to free space. Finally, a symmetric transverse cross-section ensures that the photons are emitted in a highly Gaussian transverse spatial mode.

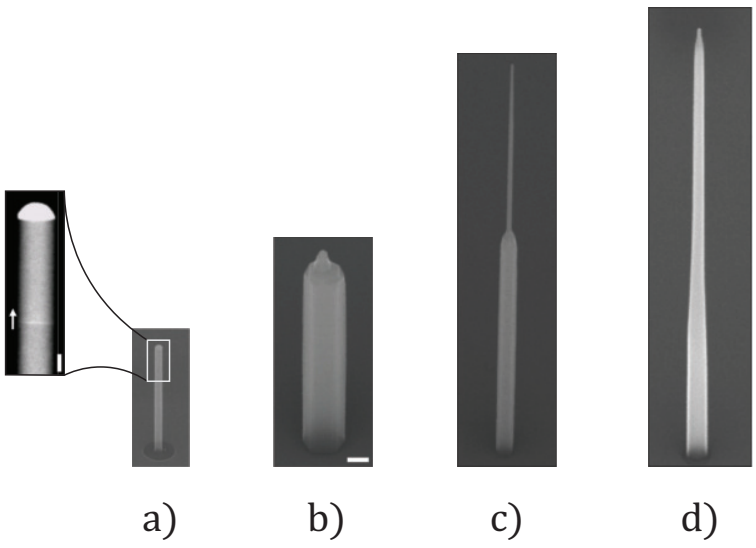


Figure 2.5: Images of the QD growth.

## 2.3 Types of Excitation

When an excitation laser with energy larger than the band gap of the InP is used to excite the quantum dot, it can be absorbed anywhere in the nanowire or the dot. It excites electrons, giving them much more energy than they need to cross the bandgap, as shown in figure 2.6. The electron loses energy through a relaxation process — a combination of interactions with different phonon modes in the surrounding lattice — and is eventually trapped in the quantum dot and falls to the lowest energy state in the dot. Similarly, there are impurities in the InP lattice with energy levels within the InP bandgap that electrons can be excited to, as illustrated in figure **??**. When the excitation laser wavelength has an energy tuned to than that of the defect, it can excite electrons in that particular spot; the excited electrons must then tunnel into the quantum dot, relaxing to the ground state by losing energy to phonon modes. In the nanowire sample investigated in this thesis, there is a strong quasi-resonant excitation present at 869.5 nm.

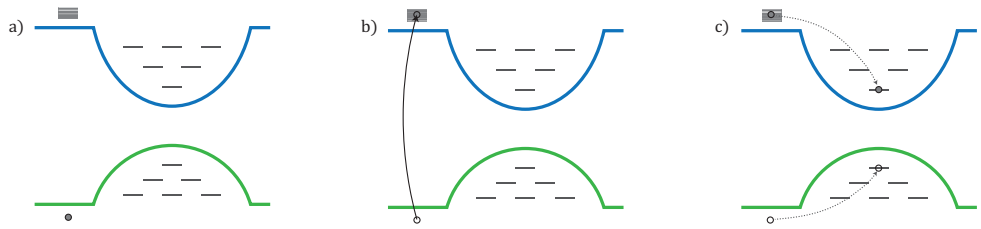


Figure 2.6: Band diagram illustration of above-bandgap excitation process: a) an electron in the valence band is b) excited to the conduction band by a laser pulse and then c) is trapped by the quantum dot and decays to occupy the s-shell energy level.

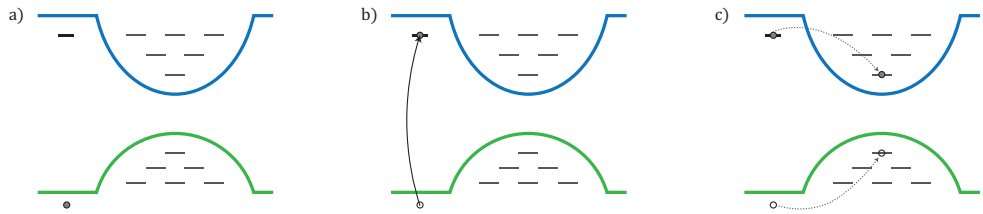


Figure 2.7: Band diagram illustration of the quasi-resonant excitation process: a) an electron in the valence band is b) excited to a defect state within the band gap and then c) is trapped by the quantum dot and decays to occupy the s-shell energy level.

Electrons can also be excited within the quantum dot. Tuning the wavelength and spectral properties of the excitation laser to coincide with one of the transitions in the quantum

dot creates a resonant excitation ending either at the exciton or biexciton state. This can be done by exciting directly to the single exciton energy level, a process called s-shell resonance, illustrated in Figure 2.8 a. Or, the quantum dot can resonantly absorb two photons at half the biexciton energy, creating two excitons and putting the quantum dot directly into the biexciton energy level, in a process called two-photon resonant excitation (TPRE) and illustrated in Figure 2.8 b. If either the center wavelength or the spectral shape of this excitation is detuned slightly, so that the state has a higher energy than the biexciton state, then a phonon-mediated process can occur, as illustrated in Figure 2.8 c.

The properties of the excitation pulse have a strong influence on the indistinguishability and multi-photon suppression of the emitted photons. This influence is mainly effected through several types of jitter, when the temporal and spectral properties fluctuate on a timescale that affects subsequent emission events. Emission time jitter — uncertainty in the emission time of the photon — will introduce distinguishability between subsequent photons. If, after the biexciton decays, another exciton falls into the quantum dot and is trapped, there will be multiple biexciton photons emitted before the quantum dot returns to its ground state (this process is called, unsurprisingly, re-excitation), which is more likely to happen for high-energy excitations. Changes in the charge environment change the electric field in the region of the quantum dot, which changes the energy of the exciton and produces spectral jitter, also makes subsequent photons more distinguishable.

Pumping on resonance with either the exciton or biexciton state creates excitons directly in the quantum dot, bypassing the trapping process and shortening the time between excitation and emission. This type of excitation eliminates the need for relaxation processes, as the excitons do not need to decay in energy and are already trapped by the quantum dot. Thus, it reduces temporal uncertainty and lowers the emission time jitter. It also significantly lowers the probability of re-excitation by creating the excitons in precisely the intended energy state. We thus expect TPRE to reduce both the emission time jitter and the re-excitation probability, and improve both the indistinguishability and the multi-photon suppression. By this same logic, moving from above-bandgap to quasi-resonant excitation should also improve the indistinguishability, because reducing the energy of the excitation pulse should lower the emission time jitter.

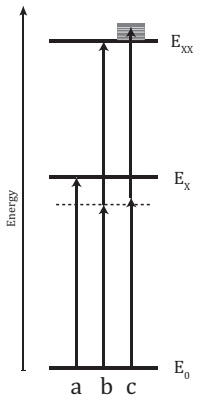


Figure 2.8: Energy level diagram depicting three processes for exciting electrons within the quantum dot: a) s-shell transition directly to the energy level of a single exciton, b) two-photon absorption process transitions directly to the biexciton state, and c) an energy-detuned, phonon-mediated two-photon excitation.

## 2.4 Exciting on Resonance

The most straightforward way to model a resonant excitation is with a two-level atom coupled to a single-mode field. Under both the dipole and rotating wave approximations, the Hamiltonian for this system can be written in two parts, $\hat{H} = \hat{H}_0 + \hat{H}_1$; the energy of the field and atom in isolation,

$$\hat{H}_0 = \hbar\nu\hat{a}^\dagger\hat{a} + \frac{1}{2}\hbar\omega\hat{\sigma}_z, \tag{2.6}$$

and the interaction energy,

$$\hat{H}_1 = \hbar g(\hat{\sigma}_+\hat{a} + \hat{a}^\dagger\hat{\sigma}_-), \tag{2.7}$$

The first term of the interaction Hamiltonian $\hat{H}_1$ describes the process of exciting one electron by absorption of a single photon from the field; the second term models that opposite process, a radiative decay that emits one photon.

We focus on the latter process, the resonant two-photon excitation, which simultaneously creates two excitons in the XX state. A resonant excitation to the XX state can be accomplished in two ways [**?** ]: either with single-photon absorption at both the $\gamma_X$ and $\gamma_{XX}$ frequencies, or by absorbing two photons at energy $E_0 - \frac{1}{2}\Delta E_B$. If the properties of the excitation pulse are tuned to be exactly resonant with the transition, the quantum dot coherently oscillates between the ground state and biexciton state. Just like any other resonant transition, the signature of this resonance is sinusoidal oscillations in the count

rate of emitted photons. In this two-photon resonant process, because the emission from the XX state is a cascade, we observe oscillations in both the biexciton and exciton photons.

We can see this mathematically by considering a slightly more complicated model than the two-level atom interacting with a single mode field. We model the two-photon absorption process with a four-level atomic configuration: ground state $|g\rangle$, two exciton states of orthogonal linear polarizations, $|X\rangle$ and $|Y\rangle$, and a biexciton state $|XX\rangle$. The Hamiltonian of this system can be written, in a frame rotating with frequency $\omega$, as [**?** ]:

$$\hat{H} = \frac{1}{2}\Delta E_B\Big( |+\rangle\langle+| + |-\rangle\langle-| \Big) + \frac{1}{2\sqrt{2}}\Big[ f(t)\Big( |g\rangle + |\mathrm{XX}\rangle \Big)\Big( \langle+| + \langle-| \Big) + \mathrm{H.c.}\Big] \quad (2.8)$$

where $f(t)$ is the envelope of the laser pulse.

$$|\Psi(t)\rangle = \frac{1}{\sqrt{2}}\left[ |1\rangle + e^{-i\Lambda(t)}\Big( c_2(t)\,|2\rangle + c_3(t)\,|3\rangle \Big)\right] \quad (2.9)$$

where $c_2(t)$ and $c_3(t)$ are coefficents that depend on the shape of the excitation pulse and the biexciton binding energy $\Delta E_B$, while the phase $\Lambda(t)$ is

$$\Lambda(t) = \frac{1}{4\hbar}\int_{-\infty}^{t} d\tau \left[ \Delta E_B - \sqrt{(\Delta E_B)^2 + 8f^2(t)} \right]. \quad (2.10)$$

Once the excitation laser pulse has been fully absorbed, the quantum dot state is no longer time-dependent, and can be expressed as [**?** ]:

$$|\Psi\rangle = \frac{1}{\sqrt{2}}\Big( |1\rangle + e^{-i\,\Lambda(\infty)}\,|3\rangle \Big) \quad (2.11)$$

$$|\Psi\rangle = e^{-i\,\Lambda(\infty)}\,\frac{1}{2}\left[ \cos\left(\frac{\Lambda(\infty)}{2}\right)|g\rangle + \sin\left(\frac{\Lambda(\infty)}{2}\right)|\mathrm{XX}\rangle \right] \quad (2.12)$$

By expressing the quantum dot state in terms of the two states of interest, $|g\rangle$ and $|\mathrm{XX}\rangle$, we can easily see that the occupation probability of the XX state is sinusoidal [**?** ]:

$$N_{XX} = \Big|\,\langle \mathrm{XX}|\Psi\rangle\,\Big|^2 = \sin^2\left(\frac{\Lambda(\infty)}{2}\right) \quad (2.13)$$

The occupation probability relates proportionally to the radiative decay, and thus, we also expect the counts of both the exciton and biexciton photons to depend sinusoidally on both the excitation power and pulse area.

# Chapter 3

# Implementing Resonant Excitation

Two-photon resonant excitation (TPRE) presents two main technical hurdles that must be overcome to successfully design the experimental setup: low photon counts, and the need to separate the emitted photons from the reflected laser.

Two-photon resonant absorption can only produce excitons in the lowest quantum dot energy level; thus, the excitation pulse can only be absorbed in the quantum dot, which has a very small volume. Therefore, only a small fraction of the excitation pulse power will be converted into excitons. We expect much fewer photons to be produced by two-photon resonant excitation than the other types of excitations, which are absorbed everywhere in the nanowire.

Because the excitation laser is very spectrally close (within 1 nm) to the exciton and biexciton photons, separating the photons from the laser reflection is a challenge. A small amount of the excitation laser reflects off the surface of the substrate, takes the same path through the collection optics as the photons emitted from the quantum dot, and is coupled into the fiber with those photons. Though it is a small fraction of the power used to excite the quantum dot, if not filtered properly, the reflected laser light is still enough to overwhelm the photons at the detector. Thus, we must suppress this laser reflection without significantly diminishing the counts of the exciton and biexciton photons.

In the first section, we give a deeper analysis of the challenges of implementing this excitation, and compare the two different techniques that we used for filtering the laser reflection. The two sections following will address each of those experimental designs in greater depth. In the final section, we present evidence that we have succeeded in implementing two-photon resonant excitation in nanowire quantum dots.

## 3.1 Design Options

An experimental setup must be chosen that collects the photons into fiber with the highest possible transmission efficiency, while thoroughly extinguishing the laser reflection. Additionally, separating the exciton and biexciton would allow us to bypass the two Princeton spectrometers that we are currently using, which have dismally low transmission efficiency that is also polarization-dependent, which is problematic for our Hong-Ou-Mandel measurement.

Within the literature, there are several predominant strategies to overcome these challenges: using polarization or spectral filtering. While polarization filtering is generally much quicker to set up, and does not require specialized optics, it by design has a very low efficiency, and will alter the polarization of the emitted photons, ruining any polarization entanglement. Spectral filtering can be implemented in two ways - with a grating, which spatially spreads the frequency components, or a band-pass filter, which selectively extinguishes a narrow range of wavelengths. Very good suppression can be achieved by using band-pass filters; in some experiments where ideal single photon source properties were desired, and thus suppressing the laser reflection was especially crucial, several identical filters were used in succession. This technique works quite well, but filters are very expensive and must be made to suit the emission of each specific dot. Thus, this relying on notch filters is highly dot-specific, and not flexible or scalable.

We implemented a photon coupling design of both kinds: polarization for the short term, and then spectral selection using a transmission grating as a more permanent setup. Though it took more effort and time to implement, the high transmission efficiency and lack of influence on the relative polarizations of the emitted photons and their entanglement made grating-based spectral filtering the best choice for a TPRE implementation that is useful in the long term to the entire research team.

## 3.2 Polarization Filtering

One strategy for eliminating the laser reflection without extinguishing the emitted photons is to use a filtering technique that only transmits light with a specific polarization .

We must excite the two-photon resonant transition with linearly polarized light in order to be able to create two excitons in the quantum dot ground state with opposite spins. The reflection of the excitation pulse remains strongly linearly polarized, while the exciton and biexciton photons are circularly polarized. Placing a linear polarizer before the fiber

coupler that is aligned orthogonally to the excitation polarization, we extinguish a sufficient portion of the laser reflection, and can easily resolve the single photon emissions on the spectrometers.

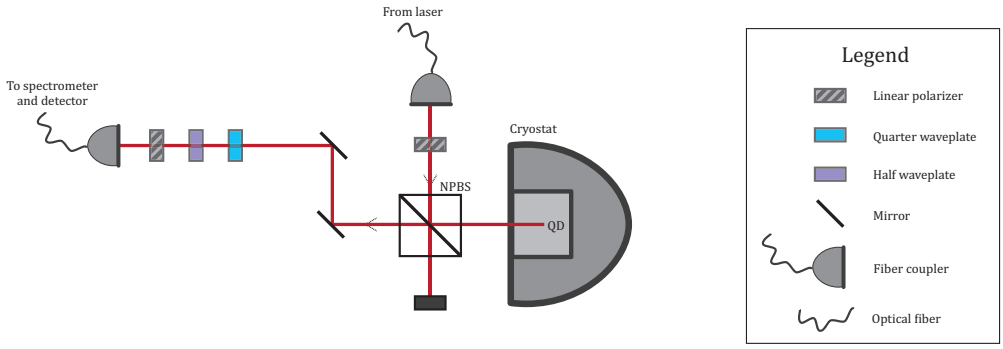


Figure 3.1: Experimental set-up to filter laser reflection using polarization, as described in the text of this section.

We added a half and a quarter waveplate before the polarizer to compensate for any polarization rotations induced by the nanowire and mirrors. Cyclic adjustment of the waveplate angles allow us to minimize the reflected laser power. Spatial filtering provided by coupling into single mode fiber is also crucial to successful suppression of the laser reflection.

This suppression technique is quick to implement and excellent as a first step, but was not sufficient for our experimental needs because of several drawbacks. The polarizer alone eliminates half of the photons produced by the quantum dot and changes the spatial mode, which significantly decreases both the fiber coupling efficiency and count rate. The photons that are collected all have identical polarization, and are no longer entangled. Entanglement produced by the biexciton-exciton cascade is a valuable resource for our lab, useful for many future investigations and necessary for the realization of a quantum repeater — thus, cross-polarized suppression of the laser reflection is not an adequate long-term TPRE implementation.

## 3.3 Spectral Filtering

As discussed in the previous section, the cross-polarized filter design was effective at suppressing the laser reflection, but also lowered the exciton and biexciton counts significantly.

Combined with other sources of transmission loss in the rest of our experimental setup, the photon count rate was too low to measure the Hong Ou Mandel interference effectively.

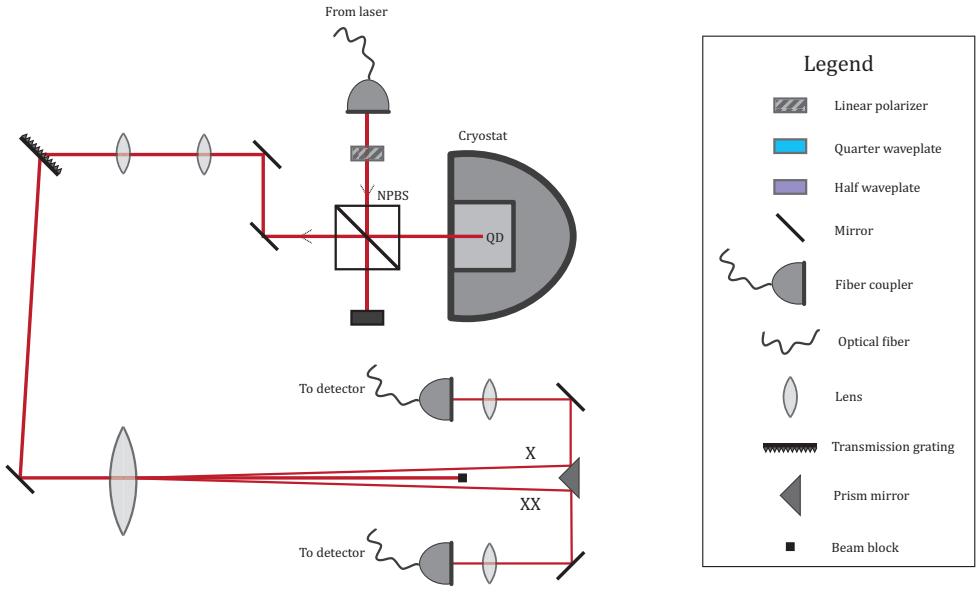


Figure 3.2: Experimental set-up to extinguish laser reflection using a grating-based spectral filter, as described in the text of this section.

We constructed a home-built spectrometer comprised of a transmission grating (LightSmyth Technologies T-1500-875 High Efficiency Transmission Grating, 1504 lines per mm at 875 nm) and a 1 meter focal length lens (ThorLabs), and placed a small hex wrench at the focus to block the laser. The grating imparts a different angular shift to the laser reflection and emitted photons, while the lens converts that angle to a focal point shifted off-center. If that displacement is larger than the beam radii of exciton and biexciton photons, then the laser can be blocked completely without attenuating either of the photon beams. Additionally, the exciton and biexciton will shift in away from each other and the laser reflection between them. A right angle prism mirror can be used to send the two photon beams in opposite directions to be coupled into different fibers.

This design has several clear advantages:

1. A transmission efficiency limited only by its constituent optical elements.
2. It does not significantly alter the relative polarization between the exciton and biexciton.

3. It circumvents the need for any other spectral filtering.

This scheme is far superior to the polarization-based design in all of our criteria. Unfortunately, despite our best alignment attempts, we were never able to completely extinguish all of the spectral components of the laser reflection. We deduced that this was caused by a partial overlap of the laser reflection and photon beams at the focal point of the lens, which could have been caused by either uncollimated emission from the cryostat, or different beam sizes of the photons and laser reflection. This could be potentially addressed by more precise alignment of the telescope (2-f system) used to enlarge the beams in order to fill as much of the useful area the grating as possible.

## 3.4 Demonstrating Resonance

As explained in Section 2.4, when the quantum dot is excited exactly on resonance with a transition, the detected counts will oscillate as a function of the excitation power. In this case, since we are exciting a two-photon transition, we expect both the biexciton and exciton counts to exhibit Rabi oscillations. As shown in Figure 3.3, Rabi oscillations are indeed observed; the smooth sinusoid-like curves and large amplitude of the oscillation indicate that the center frequency and spectral width of the excitation are very near the true resonance of the transition.

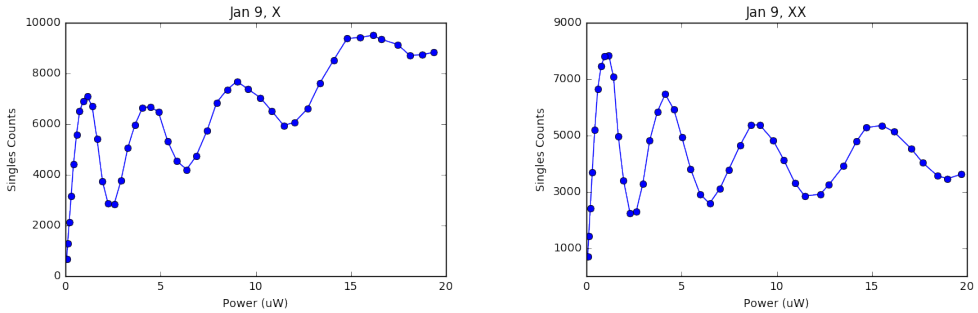


Figure 3.3: Detected single photon counts of both the a) exciton (X) and b) biexciton (XX). Both plots show clear oscillations as a function of the excitation power.

# Chapter 4

# Characterizing Multi-Photon Suppression

In an ideal single photon source, the stream of photons is evenly spaced. At any given time, one and only one photon arrives at the detector, and the photons are detected at regular intervals. But most sources are not ideal, and we need a way to characterize the temporal distribution of the photons produced by any particular source. This chapter formalizes that characterization, and presents the experimental measurement that allows us to characterize real sources.

We first qualitatively describe the ways to classify light based on the temporal distribution of photons in a beam. Then, in the next two sections, we introduce the second-order autocorrelation function ($g^{(2)}(\tau)$), which quantifies this classification, and the Hanbury Brown-Twiss interferometer, which can be used to experimentally measure the autocorrelation function. In the next section, we analyze the autocorrelation function with the operator tools of quantum optics to gain a greater understanding of the expected outcome of our measurements. In the final section, we present measurements of the second-order autocorrelation under two different types of excitation and the $g^{(2)}(0)$ values calculated from these histograms, comparing these results to better understand the effect of excitation type on the multi-photon suppression.

## 4.1 Temporal Distribution of Photons in a Beam

We can characterize a beam of light in three ways based on its temporal distribution of photons: random, bunched, and anti-bunched. This section will give a qualitative description of these three types of light.

The photons in a beam of light can be distributed randomly, with an equal probability of

finding a photon at every time interval. The probability of finding photons can also be temporally non-uniform in two ways. The photons could be 'bunched' together, with high probabilities of measuring a photon clustered together at particular times. In a bunched photon distribution, if there is a photon in a time interval, there is a much higher probability of measuring photons soon after. Conversely, the photons could be spread out, with the presence of a photon in a time interval lowering the probability of measuring photons soon after. This is the opposite of a bunched distribution; the 'anti-bunched' photons are produced at regular intervals, and are distributed evenly in a beam.

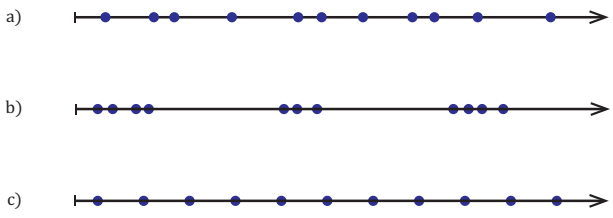


Figure 4.1: Conceptual illustrations of three broad types of temporal distributions of photons within a beam of light: a) random, b) bunched, c) anti-bunched. Each dot represents a photon. (figure adapted from [5])

## 4.2 Second-Order Autocorrelation Function

Most kinds of light can be completely described by Maxwellian electromagnetic waves. In this classical picture, the coherence properties of a beam are related to its intensity fluctuations [5]. Larger intensity fluctuations will lower the coherence, as the light is less stable, and it is less likely for the properties of the light at any particular pair of points in the beam to be correlated. A beam of light can be categorized as random, bunched, or anti-bunched by measuring its second-order autocorrelation function, $g^{(2)}(\tau)$ [5].

The second-order autocorrelation function quantifies the correlations in intensity at two points of the beam, specified by times $t$ and $t+\tau$:

$$g^{(2)}(\tau) = \frac{\langle\langle I(t)\, I(t+\tau)\rangle\rangle}{\langle\langle I(t)\rangle\rangle\, \langle\langle I(t+\tau)\rangle\rangle}, \tag{4.1}$$

where $\langle\langle \cdots \rangle\rangle$ is a statistical average over a time $T$, which is long relative to time delay $\tau$:

$$\left\langle\left\langle f(t) \right\rangle\right\rangle = \frac{1}{T}\int_T f(t)\, dt, \tag{4.2}$$

defined for an arbitrary function $f(t)$ [5]. Thus, in the classical interpretation, the second-order autocorrelation function provides a measure of the coherence and stability of the beam.

For a perfectly coherent, monochromatic beam of constant intensity, the second-order autocorrelation function will be constant: $g^{(2)}(\tau) = 1$ for all delay values $\tau$ [5]. Thus, the light at any two pairs of points in the beam is coherent, and there are no discontinuities in the phase. This is the most stable beam that can be accurately described with classical optical theory, and it serves as a threshold for non-classical light: if the second-order autocorrelation function of a beam has $g^{(2)}(0) < 1$, it cannot be described with classical theories of optics, and can only be characterized as quantum.

However, perfectly monochromatic light with a constant intensity and infinite coherence is quite unrealistic. All real and easily producible sources of classical light have a finite coherence length, and thus have a non-constant $g^{(2)}$ function. Sources like these are often called chaotic, because the underlying processes that produce the intensity fluctuations are random. Discontinuities in the phase of the light caused by, for example, atomic collisions or random decay, reduce the coherence on long timescales and cause the intensity to be more highly correlated ($g^{(2)} > 1$) at small delay values. An example of a chaotic source with an easily computable $g^{(2)}$ function is atomic discharge, in which gaseous atoms are excited by an electric current and then emit light by spontaneous radiative decay. Atomic discharge sources with Doppler-broadened spectral lines have a Gaussian autocorrelation function [5]:

$$g^{(2)}(\tau) = 1 + e^{-\pi\left(\frac{\tau}{\tau_c}\right)^2}, \tag{4.3}$$

while light sources that are predominantly broadened by the lifetime of the excited state have a Lorentzian autocorrelation function [5]:

$$g^{(2)}(\tau) = 1 + e^{-\frac{2|\tau|}{\tau_0}}, \tag{4.4}$$

where $\tau_c$ is the coherence time and $\tau_0$ is the excited state lifetime [5].

In general, for all chaotic sources, the second-order autocorrelation value decays with increasing delay time, and $g^{(2)}(\tau) \leq g^{(2)}(0)$ [5]. This suggests that the coherence decays over time, as the time delay $\tau$ increases. The second-order autocorrelation function cannot

take on values less than one when evaluated with a classical description of light; thus, $g^{(2)}$ values less than one do not have a meaningful interpretation in terms of coherence.

For all types of classical light, the second-order autocorrelation function will always have $g^{(2)}(0) \geq 1$. Furthermore, all sources of light with fluctuating intensity, such as chaotic beams and thermal radiation, will have $g^{(2)}(0) > 1$ [5]. When evaluated with quantum theory, both the chaotic sources described above and all sources of classical light with finite coherence will show a bunched temporal distribution of photons. The higher the $g^{(2)}(0)$, the more likely it is to find many photons 'bunched' together, and those 'bunches' are more likely to have a short duration.

## 4.3 Hanbury Brown-Twiss Experiment

A straightforward and accurate way to measure the second-order autocorrelation function uses a Hanbury Brown-Twiss (HBT) apparatus, which consists of a beamsplitter and two single photon detectors, one placed on each path. This setup was first realized by Hanbury Brown and Twiss in 1956 [8], in order to improve on the Michelson stellar interferometer [12]. Measuring the correlations between intensities registered on the two photodiodes allowed the Hanbury Brown and Twiss experiment more stability and higher resolution than the Michelson interferometer, which relied on measuring the interference fringe visibility. This new design allowed Hanbury Brown and Twiss to measure much larger star diameters to a higher accuracy than Michelson [5]. But, as we will explore in Section **4.4** , this experimental design also became useful for measuring properties of quantum light.

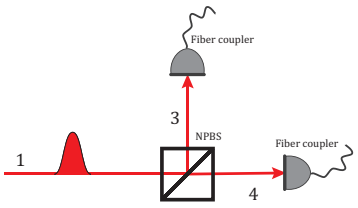


Figure 4.2: Idealized Hanbury Brown Twiss apparatus, showing an incoming beam (in red, mode 1) split on a 50/50 nonpolarizing beamsplitter, and a detector on each of the beamsplitter outputs (modes labeled 3 and 4).

## 4.4 Second Order Autocorrelation Function with Photons

If we treat the input fields as streams of photons, we can use the linear relationship between average intensity and number of photons to rewrite equation 4.1 in terms of the photon number operators on each path, $\hat{n}_i$ [5]:

$$g^{(2)}(\tau) = \frac{\left\langle\!\left\langle \hat{n}_1(t)\hat{n}_2(t+\tau) \right\rangle\!\right\rangle}{\left\langle\!\left\langle \hat{n}_1(t) \right\rangle\!\right\rangle \left\langle\!\left\langle \hat{n}_2(t+\tau) \right\rangle\!\right\rangle} \tag{4.5}$$

where the angle brackets indicate both statistical averaging over a long time $T$ (as specified in equation 4.2) and also the quantum expectation value.

The numerator of equation 4.5 quantifies the correlations between the counts registered at the two detectors, specifically the average number of times both detectors register a photon separated by a time delay $\tau$, normalized by the product of the average counts at each detector. By correlating the time of arrival of the photons detected on the two paths, we can calculate $\tau$ for each pair of detected photons and measure in coincidence, producing a histogram of correlation counts based on the time delay between the two detectors registering counts.

We express the input field in the Fock basis as:

$$\rho = \sum_{n,n'} \rho_{n,n'} \; |n\rangle \langle n'| \;\; , \tag{4.6}$$

where $\rho_{n,n'}$ are the diagonal elements of the density matrix in the Fock basis. As we show in Appendix A, the second order autocorrelation function for this general input state can be written as:

$$g^{(2)}(0) = \frac{\sum_n p_n \, n(n-1)}{\left( \sum_n p_n \, n \right)^2} \;\; . \tag{4.7}$$

where $p_n = \rho_{n,n}$. We can also calculate how we expect the $g^{(2)}$ function to depend on the photon number state of the input field, assuming that it is in a pure Fock state, $|\Psi\rangle = |n\rangle$, and not the vacuum state, $n \geq 1$ [5]:

$$g^{(2)}(0) = \frac{n-1}{n} \;\; . \tag{4.8}$$

Every pure photon number state must have a second-order autocorrelation value less than one, $g^{(2)}(0) < 1$. But, as we can see from equation 4.8, only a single photon ($n = 1$) state can have $g^{(2)}(0) = 0$. Thus, the $g^{(2)}(0)$ value quantifies how close to an ideal single photon source a particular source of light is, assuming that it is in a pure Fock state.

If the source truly produces only one photon at a time, there will be no coincidence counts registered at zero time delay, because a single photon cannot be detected on both paths after the beamsplitter. A perfectly antibunched photon stream, therefore, will have a $g^{(2)}(0)$ of exactly zero. The closer to zero the $g^{(2)}(0)$ value, the less randomly spaced the photons are, and thus, the better the single photon source. If a source emits an approximately deterministic single photon stream, it will have a very low $g^{(2)}(0)$ value - it is known with high probability both each photon will be emitted and that it will be alone. Measuring coincidence counts at zero time delay indicates that, at least some of the time, the source emits pulses containing more than one photon, and it is not an ideal single photon source.

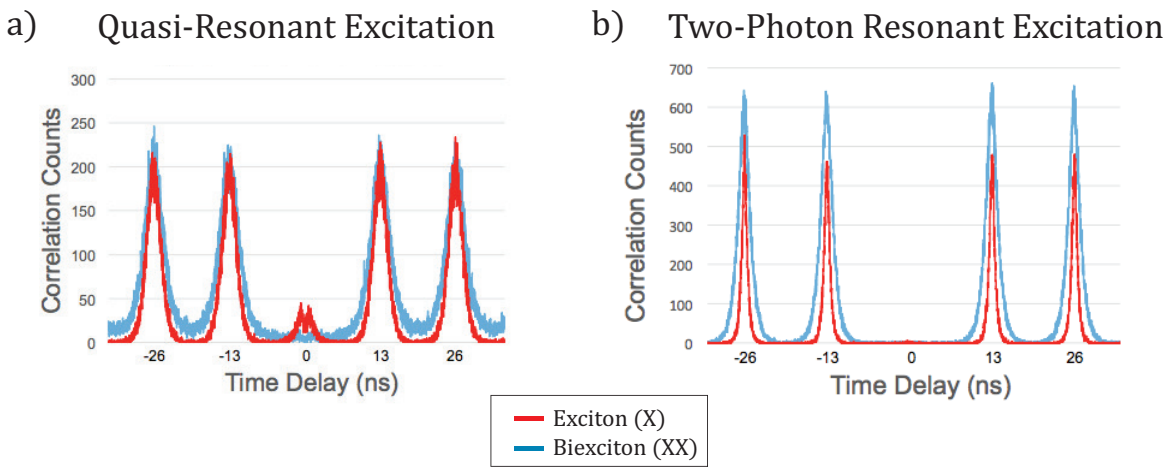


Figure 4.3: Second order autocorrelation measured under a) quasi-resonant and b) two photon resonant excitation excitation. (Data for (a) collected by Arash Ahmadi.)

## 4.5 Measuring Autocorrelation

Our excitation laser is pulsed, and thus, we expect the photons to be produced at specific times and the coincidence histogram to be a series of regularly spaced peaks separated by the repetition rate of the exciting laser. The peaks are broadened by the intrinsic lifetime of the exciton in the quantum dot, while the laser pulses have a Gaussian temporal distribution; thus, the peaks will be a convolution of a Lorentzian and Gaussian. To extract a $g^{(2)}(0)$ value from the autocorrelation histogram in a pulsed scenario, we integrate the counts in the central peak (in this thesis, this quantity is referred to as the 'peak area'). We then normalize the central peak area by an average of the peak areas at large time delay. To calculate $g^{(2)}(0)$, we integrate all the counts in a time window surrounding $\tau = 0$

of width $\delta\tau$, and normalize by the total counts in the same time window in an average side peak ($\tau \neq 0$).

From the data presented in Figure 4.3a, we extract a $g^{(2)}(0)$ value of $4.7 * 10^{-3}$ for the exciton photon and $7.5 * 10^{-3}$ for the biexciton photon. This shows excellent multi-photon suppression and thus, our quantum dot sample fulfills one of the essential and most important properties of a single photon source: it produces single photons in a Fock state $|1\rangle$ with a very high probability.

Arash Ahmadi measured the histogram shown in Figure 4.3b from the same sample excited quasi-resonantly, and extracted $g^{(2)}(0)$ values of 0.05 for the exciton photon and 0.17 for the biexciton photon. Under two-photon resonant excitation, the exciton $g^{(2)}(0)$ value is similar to that measured under quasi-resonant excitation, but the biexciton $g^{(2)}(0)$ is markedly lower. This is primarily because the resonant excitation eliminates re-excitation processes by creating two excitons directly into the biexciton state. We can also see by visually comparing the widths of the peaks in the two autocorrelation measurements that the lifetime of both biexciton and exciton states decreases under two-photon resonant excitation. Thus, exciting with TPRE significantly improves the multi-photon suppression of our sample, making it a much better single photon source.

Table 4.1: Measured $g^{(2)}(0)$ Values

| Excitation Type | Exciton | Biexciton |
|---|---|---|
| Quasi-Resonant | 0.05 | 0.17 |
| Two-Photon Resonant | 0.0047 | 0.0075 |

Comparison of second-order autocorrelation ($g^{(2)}(0)$) value measured under two types of excitation, quasi-resonant and two-photon resonant, calculated from the correlation histograms shown in Figure 4.3, at full peak integration $\delta\tau = 6$ ns.

# Chapter 5

# Measuring Indistinguishability

## 5.1 Indistinguishability

In quantum theory, particles are described by their probability amplitudes in certain attributes, such as position, momentum, spin, and energy. If all of the attributes of two particles take on identical amplitudes, then the particles themselves are indistinguishable, and cannot be differentiated from each other. We can understand light as a collection of massless particles called photons. The measurable attributes of photons relevant to this thesis are:

1. **Temporal mode**, the shape and amplitude of the probability distribution of the photon in the time domain.
2. **Spectral mode**, the probability distribution in the frequency domain.
3. **Transverse spatial mode**, the distribution of intensity in the plane perpendicular to the direction of propagation.
4. **Polarization**, the spin of the photon.
5. **Propagation direction**, the direction of travel — equivalently, the orientation of the photon's momentum.
6. **Time of arrival** at either an optical element or a detector.

If the probability distributions associated with all of the attributes of both photons are identical, then the two photons are indistinguishable.

## 5.2 Hong-Ou-Mandel Effect

The Hong-Ou-Mandel (HOM) effect describes the interference of two single photons incident on different input ports of a non-polarizing beamsplitter. First discovered in 1987, this effect was utilized by C. K. Hong, Z. Y. Ou, and L. Mandel to measure the time duration of picosecond pulses with femtosecond precision. This section will give an overview of the HOM effect, starting with a brief description of the original 1987 experiment, followed by a more thorough examination of the mathematical underpinnings of this interference effect.

If the photons are completely identical in all of the attributes described in Section 5.1, the amplitudes for the photons to leave the beamsplitter at different ports will destructively interfere, and no coincidences will be detected. Conversely, if the photons are partially distinguishable, the amplitudes for coincidence will not fully cancel. By translating the beamsplitter position to alter the relative path lengths and measuring the change in coincidence counts, Hong, Ou, and Mandel measured the length of a very short pulse with much higher resolution than was previously possible [9]. The HOM interference effect can also be used to measure the degree of indistinguishability of two photons, as we explore in the remainder of this section.

We will now examine the Hong Ou Mandel interference effect in detail, using polarization as the degree of freedom that introduces distinguishability. To simplify the calculation, we assume, for now, that we can experimentally control all photon attributes, and that all photon attributes besides polarization are completely identical when the photons encounter the beamsplitter.

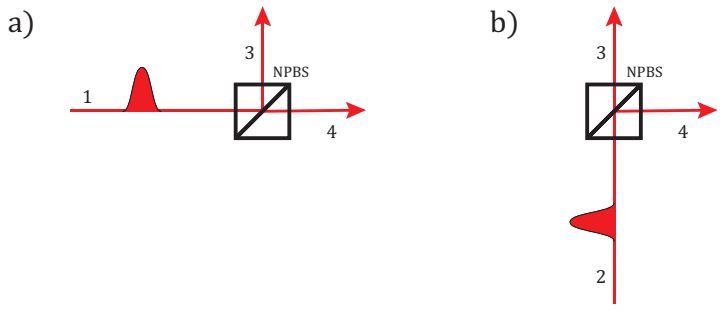


Figure 5.1: The action of a non-polarized beamsplitter, transforming a photon incident in modes a) 1 and b) 2 into a superposition of output modes 3 and 4 with different phases, as described in Equations 5.1 and 5.2.

The action of a non-polarizing beamsplitter on incoming modes can be modeled as a unitary transformation $\hat{U}_{BS}$ acting on the creation operators, $\hat{a}_1^\dagger$ and $\hat{a}_2^\dagger$, transforming a photon in either input mode into superpositions of photons in both output modes:

$$\hat{U}_{BS}\ \hat{a}_1^\dagger = \sqrt{p_r}\,\hat{a}_3^\dagger + \sqrt{p_t}\,\hat{a}_4^\dagger, \tag{5.1}$$

$$\hat{U}_{BS}\ \hat{a}_2^\dagger = \sqrt{p_t}\,\hat{a}_3^\dagger - \sqrt{p_r}\,\hat{a}_4^\dagger, \tag{5.2}$$

where $p_r$ is the probability of reflection, $p_t$ is the probability of transmission, and, to preserve unitarity, $p_r + p_t = 1$.

When two photons are incident on a non-polarizing beamsplitter, one at each input port, there are four possible outcomes, corresponding with each photon either reflecting or transmitting:

$$\hat{U}_{BS}\ \hat{a}_1^\dagger\,\hat{a}_2^\dagger\ |0\rangle_1\,|0\rangle_2 = \left(\sqrt{p_r}\,\hat{a}_3^\dagger + \sqrt{p_t}\,\hat{a}_4^\dagger\right)\left(\sqrt{p_t}\,\hat{a}_3^\dagger - \sqrt{p_r}\,\hat{a}_4^\dagger\right)|0\rangle_3\,|0\rangle_4 \tag{5.3}$$

$$= \left[\sqrt{p_r\,p_t}\left(\hat{a}_3^\dagger\hat{a}_3^\dagger - \hat{a}_4^\dagger\hat{a}_4^\dagger\right) + p_t\,\hat{a}_4^\dagger\hat{a}_3^\dagger - p_r\,\hat{a}_3^\dagger\hat{a}_4^\dagger\right]|0\rangle_3\,|0\rangle_4\,. \tag{5.4}$$

This gives two categories of output states: either the photons cluster at the same output port,as in the first two terms of Equation 5.4, or the photons split, leaving the beamsplitter from different ports, as in the last two terms of Equation 5.4.

If we place a single photon detector at each output of the beamsplitter, and the beamsplitter is balanced ($p_r = p_t = 0.5$), we expect the following outcomes: 25% of the time we put photons into the beamsplitter, we receive a click in only one of the detectors; another 25% of the time, we receive a click only in the other detector; while the final 50%, we receive clicks in both detectors simultaneously. These detectors can only distinguish between the presence and absence of photons, not the number of incident photons; thus, there will only be one click, even when more than one photon is absorbed.

If these two photons have the same polarization, the amplitudes for the two categories of possibilities (clustering and splitting) will become identical. Because of their opposite signs, the two splitting terms will cancel, ensuring that no coincidences are counted.

If the photons are orthogonally polarized at the input ports, $\hat{a}_{1,\mathrm{H}}^\dagger\ \hat{a}_{2,\mathrm{V}}^\dagger\ |0\rangle_1\,|0\rangle_2$, then after a balanced, non-polarizing beamsplitter, the state will become:

$$\hat{U}_{BS}\ \hat{a}_{1,\mathrm{H}}^\dagger\ \hat{a}_{2,\mathrm{V}}^\dagger\ |0\rangle_1\,|0\rangle_2 = \frac{1}{\sqrt{2}}\left[\hat{a}_{3,\mathrm{H}}^\dagger\ \hat{a}_{3,\mathrm{V}}^\dagger - \hat{a}_{4,\mathrm{H}}^\dagger\ \hat{a}_{4,\mathrm{V}}^\dagger + \hat{a}_{4,\mathrm{H}}^\dagger\ \hat{a}_{3,\mathrm{V}}^\dagger - \hat{a}_{3,\mathrm{H}}^\dagger\ \hat{a}_{4,\mathrm{V}}^\dagger\right]|0\rangle_3\,|0\rangle_4\,. \tag{5.5}$$

The splitting amplitudes are now distinguishable, and the full 50% of coincidences should occur. By extension, photons that are partially orthogonal at the beamsplitter input port

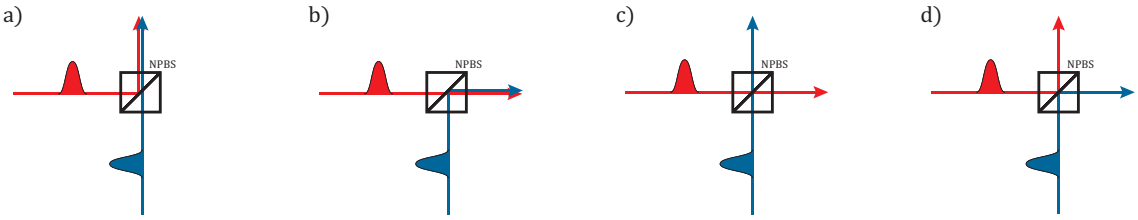


Figure 5.2: The four possible paths taken by two photons incident on a non-polarized beamsplitter: clustering (paths a and b), and splitting (paths c and d). Figure inspired by [2]; colors used for clarity in illustrating the paths of the photons.

will give splitting amplitudes that are partially distinguishable, and thus some coincidences will occur, but measurably fewer than the fully distinguishable case.

The number of coincidences that are registered over many repetitions are directly related to the degree of indistinguishability of the two photons. Thus, the indistinguishability between the two input photons can be quantified by the amount that the coincidences are extinguished, or, equivalently stated, the amount that the photons interfere destructively at the beamsplitter.

## 5.3 Experimental Apparatus

We excite the quantum dot with a sequence of regularly spaced laser pulses, and it emits a stream of highly antibunched single photons. This was verified in chapter 4 with second-order autocorrelation measurements that produced a very low $g^{(2)}(0)$ value. To measure the indistinguishability of any pair of these photons, the pair must arrive at the two input ports of a non-polarizing beamsplitter at exactly the same time. Thus, the earlier photon must be delayed by a length matching the time difference between the emission of the two photons. It is most practical, therefore, to interfere subsequent photons (i.e. photons that are emitted in neighboring pulses), because there is the shortest time difference between their emissions.

We introduce this time delay with an unbalanced Mach-Zender interferometer, shown in Figure 5.3, where the difference in path length is equal to the length that a photon travels in the temporal separation of the excitation laser pulses. The interferometer is built entirely in free space; the path of a photon through the interferometer is the following:

1. A photon is launched into the interferometer from a fiber.

2. The photon is split by a polarizing beamsplitter either onto the direct (short) or delay (long) paths, with horizontal or vertical polarization, respectively.

3. If the photon is reflected at the polarizing beamsplitter, it will take a folded delay path. We fine-tune the spatial overlap at the recombining beamsplitter by adjusting the alignment of the two mirrors, and the length of the delay arm by adjusting the translation stage.

4. If the photon is on the delay path, its polarization is adjusted by a half-waveplate mounted in a motorized stage; it will be either cross-polarized or co-polarized with the photon on the direct path, depending on the waveplate angle setting.

5. The photon encounters a non-polarizing beamsplitter, potentially combining with a photon that took the opposite path and producing interference.

6. After emerging from the recombining beamsplitter, the photon is coupled into a fiber, and conducted to a spectrometer and, finally, a detector.

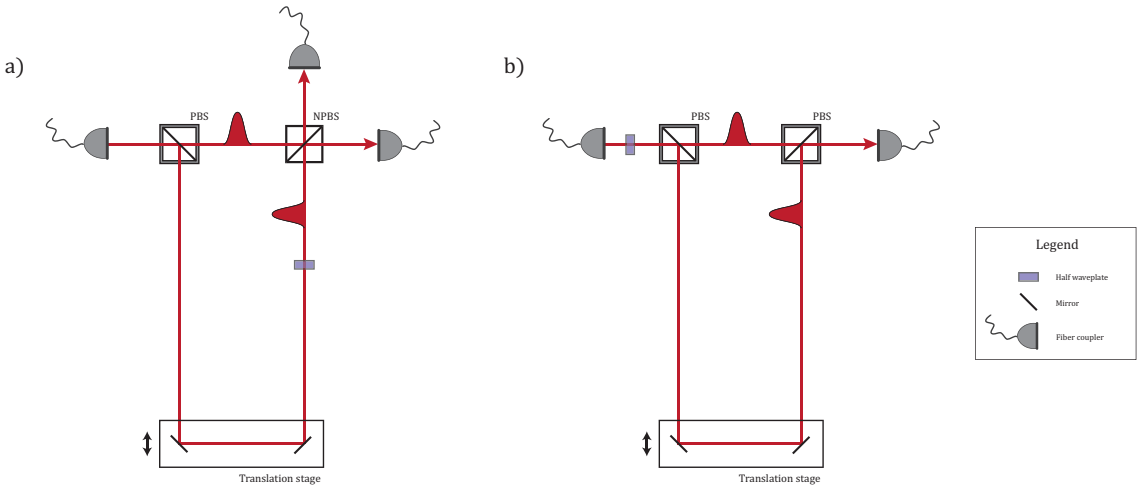


Figure 5.3: Unbalanced free space Mach-Zender interferometers for a) measuring Hong-Ou-Mandel interference, and b) doubling the repetition rate of the excitation laser(delay paths not to scale).

The longer the delay path, the more difficult it is to align the interferometer and the more likely the delay path will be temporally unstable. Temperature and humidity variations, as well as airflow in the vicinity of the experiment, can cause the optical elements and their

mounts to move, deflecting the beam from its previously aligned path and causing fluctuations in the spatial overlap of the photons at the beamsplitter. The HOM interferometer was first constructed on a raised breadboard which warped after a year in the lab; we discovered this warping after noticing that the delay alignment was unstable and fluctuated with temperature, mechanical perturbations, and over relatively short timescales (hours). This anecdote illustrates the sensitivity of a 2 meter delay to physical perturbation. Rebuilding the interferometer and firmly securing it to the table, thus eliminating the impact of the warped breadboard, significantly decreased but did not eliminate the sensitivity. For ease and precision of alignment, we chose to design this interferometer with the shortest possible delay path.

The laser emits a regular train of pulses at 76 MHz, which makes subsequent photons separated by 13 ns, or 4 meters when the pulses propagate in free space. This is quite long, and makes the delay difficult to align. We double the repetition rate to 152 MHz, in order to shorten the length of the delay arm of the interferometer. We accomplish this by passing the excitation laser through an unbalanced Mach-Zender interferometer, shown in Figure 5.3. The second polarizing beamsplitter recombines the pulses into one fiber coupler, while a half-waveplate placed before the first beamsplitter balances the power in the two arms of the interferometer. At the output of this Mach-Zender interferometer, the pulses will be 6.5 ns, or 1.964 meters, apart; this is a much easier length to align.

In order to truly measure the indistinguishability of the photons as they are emitted from the source, we must work to eliminate all sources of distinguishability introduced by the interferometer; our success in this endeavor depends largely on the quality of our interferometer design and on the precision of the alignment. Specifically, we must carefully align the spatial overlap and momenta of the photons at the recombining beamsplitter, ensure that the fiber coupling efficiencies of all four paths are balanced, and calibrate the length of the delay path to exactly match the repetition rate.

After the detectors register a photon, the following must occur:

1. The Excelitas SPCM-ARQH avalanche photodiode detector converts the photon into an electrical pulse.

2. The time tagger records its time stamp.

3. Software computes the delays between this photon and all photons previously registered at the other detector.

4. A histogram is formed by accumulating these time delays over many repetitions of the experiment.

Since the laser excites the quantum dot with regularly spaced pulses, we expect the HOM coincidence histogram to be a series of regularly spaced peaks, with temporal separation determined by the repetition rate, $\Delta$, of the excitation laser. Just as in the second-order autocorrelation measurements presented in chapter 4, the width of the peaks in the correlation histogram will be determined by the lifetime of either the exciton or biexciton, depending on which photon we are measuring. Similarly, the peaks will be broadened by the lifetime of the state that we are measuring, and the peak shape will be a convolution of a Gaussian and Lorentzian.

The two interfering photons can take multiple paths through the interferometer and still produce coincidences at the same time delay. There are many ways for pairs of photons to make coincidences separated by $\tau = n\,\Delta$ where $n \in N$), but there is only one combination of paths that can form a coincidence at $\tau = 0$. We calculate combinatorially the number of possible path combinations for each time delay category: $\tau = 0$, $\tau = \Delta$, and $\tau = n\,\Delta$ ($n \in Z, |n| \geq 2$). The results give us the ratios we should expect between the total counts in the peaks of a histogram produced by ideal, completely distinguishable photons. Similarly, the HOM effect will tell us how we should expect that ideal histogram to be modified based on the indistinguishability of the two photons.

## 5.4 Measuring Hong-Ou-Mandel Interference

To determine the HOM interference visibility, we must collect at least two histograms: one when the two photons are completely indistinguishable and the other when they are entirely distinguishable. We use polarization to control the distinguishability in this interferometer. This corresponds to measuring coincidences at two different half-waveplate settings: 45° for indistinguishable polarizations (co-polarized photons), and 0° for completely distinguishable polarizations (cross-polarized photons). Even when the polarizations are completely indistinguishable, there may still be distinguishability in the other degrees of freedom; indeed, we are using the HOM interference to measure exactly the degree of this distinguishability.

The HOM histograms shown in Figure 5.4 are far from ideal data. The asymmetry in the peaks at $\tau = \pm\Delta$, the dramatic difference in heights of normal peaks of the co- and cross-polarized histograms, and the high background counts in both histograms are all deviations from an ideal Hong-Ou-Mandel interference measurement. We now explore the sources of these deviations, which are all from the experimental design and alignment.

The asymmetry of the $\pm\Delta$ peak heights is caused by a slightly unequal reflection and

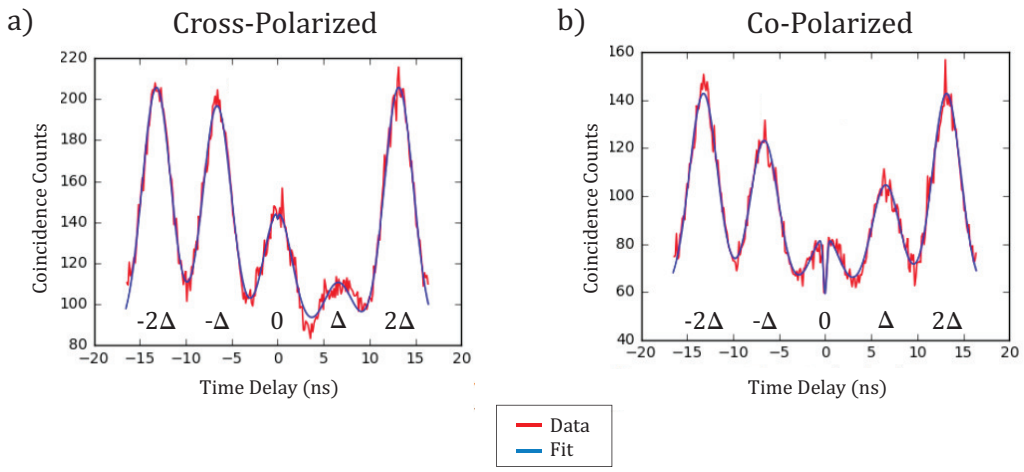


Figure 5.4: Histogram from the measurement of the Hong Ou Mandel interference under quasi-resonant excitation; measured data in red, fit in blue.

transmission coefficients of the beamsplitters, and by unbalanced coupling efficiencies of the four paths of the interferometer. The $\pm\Delta$ peak symmetry could be significantly improved by redesigning the interferometer to use a fiber beamsplitter; the coupling efficiencies are equal for all paths and the overlap at the beamsplitter is not dependent on alignment.

The difference in counts of the $\pm 2\Delta$ peaks and the change in asymmetry of the $\pm\Delta$ peaks between cross- and co-polarized histograms is caused by the polarization dependence of the spectrometers. This could be circumvented by implementing a set-up that would filter the exciton and biexciton photons from the laser reflection before the HOM interferometer, so that only one spectrometer is needed, and any polarization dependence in the spectrometer does not affect the HOM coincidence counts. We could also build a spectrometer with a transmission grating that has a smaller polarization dependence.

We have not completely pinpointed the source of the large background counts. Much of the offset seen in the histograms can be attributed to the overlap of the peaks. But, some background still remains which cannot be explained by either detector dark counts or background.

We calculate the interference visibility from the two histograms shown in Figure 5.4 by integrating the counts in the central ($\tau = 0$) peak, and normalizing by the average of the $\tau = \pm 2\Delta$ side peaks. In this way, we find the peak area ratios: $P_\perp$ (cross-polarized) and $P_\parallel$ (co-polarized). We use these peak area ratios to calculate the indistinguishability [16, 17]:

$$V = \frac{P_\perp - P_\parallel}{P_\perp} \,. \tag{5.6}$$

Table 5.1: HOM Interference Visibilities: Comparison Between Temporal Post-Selection Widths

| Temporal postselection width | 6 ns | 64 ps |
|---|---|---|
| Visibility | 30.6% | 75.9 % |

Comparison of measured HOM interference visibilities measured under quasi-resonant excitation for different lengths of temporal post-selection.

## 5.5 Discussion

We now compare the Hong-Ou-Mandel interference visibility measured under quasi-resonant excitation presented in the previous section to that of a similar sample measured under a different type of excitation. Specifically, we compare the results of our HOM interference measurement to results obtained by Reimer et. al. [13], who measured the HOM interference visibility of a quantum dot in a nanowire excited with above-bandgap light.

There are some significant differences in the experimental setup, both the Hong Ou Mandel interferometer and excitation implementation. [13] built an unbalanced Mach-Zender interferometer in fiber, utilizing a fiber beamsplitter and a fiber delay, while we built our HOM interferometer entirely in free space. But, like our experimental set-up, [13] used spectral filtering before the HOM interferometer to select the particular photon emission (exciton or biexciton) that they were to measure.

The HOM interference histograms measured under both excitation types have a very similar shape, both in their general peak shape and the width of the dip in the indistinguishable case. However, the visibilities listed in Table 5.2 show that quasi-resonant excitation does not improve the indistinguishability significantly. The quasi-resonant excitation does decrease the temporal jitter by decreasing both the energy of the free charge carriers and the time required for the quantum dot to trap charge carriers. However, it does not eliminate the jitter, leaving a jitter much longer than the photon's temporal length, and thus, also much longer than the time over which subsequent photons will interfere at the beamsplitter. To improve the indistinguishability of this source, the temporal jitter must be decreased significantly by implementing a resonant excitation.

Table 5.2: HOM Interference Visibilities: Comparison Between Excitation Types

| Type of excitation | Full peak | 64 ps |
|---|---|---|
| Above-bandgap | 8.4 % | 85 % |
| Quasi-resonant | 30.6 % | 75.9 % |

Comparison of HOM interference visibility measured under two types of excitation: above-bandgap (at excitation power $\frac{1}{5}P_{\text{sat}}$) [13] and quasi-resonant. Corresponding coincidence histograms presented in figure 5.4 and [13], and visibility calculated according to equation 5.6.

# Chapter 6

# Future Work

## 6.1 Improving the Two-Photon Resonant Excitation

Some improvements that are necessary to make our implementation of the two-photon resonant excitation stable and reproducible:

1. Improve the stability of the excitation laser power by implementing active power stabilization on the laser.
2. Improve laser mode-locking stability with better intra-cavity alignment. This should increase the intra-cavity CW power, making the spectral properties of the pulse more stable once mode-locking is achieved, and lessen the likelihood that laser loses mode-locking.
3. Improve the precision of the $N_2$ flow pressure gauge, to allow better monitoring and stabilizing of the laser cavity atmospheric humidity.
4. Improve the alignment of the pulse slicer to ensure that no chirp is added to the pulse, and to give more precision to the pulse width adjustment.
5. Implement selection of pulse spectral characteristics with EOM instead of slit; add active control to the EOM so excitation spectral qualities can be stabilized.
6. Improve the spectral suppression of the laser reflection so that spectrometers are not needed after the HOM interferometer.

If all of these improvements can be successfully implemented, they will significantly improve our ability to fine-tune the excitation pulse properties, allowing us to optimize the two-photon resonant excitation and maximize the emitted counts at the $\pi$ pulse. It will also substantially improve the temporal stability of the excitation pulse, allowing us to run measurements for much longer. Together, these improvements will make a successful HOM intereference measurement of the two-photon resonant excitation much more likely.

## 6.2 Improving the Hong-Ou-Mandel Interferometer

The main unsolved challenges of our Hong-Ou-Mandel interference measurement are the instability of three parts of the experiment: the laser, excitation pulse characteristics, and the interferometer. Together, fluctuations in these components limit both the length and accuracy of the measurement. However, TPRE produces very low counts, and thus requires a long measurement time in order to accumulate acceptable statistics. These competing demands have prevented us from measuring the indistinguishability of the photons produced under two-photon resonant excitation.

In the previous section, we listed many strategies to increase the stability and optimize the properties of the two-photon resonant excitation. In addition to all of those ideas, the detected count rate could be significantly improved by increasing the efficiency of fiber-to-fiber couplers, thereby reducing photon loss when transitioning between the many parts of the experimental setup. In the rest of this section, we propose an alternative HOM interferometer design to improve the stability of the components and repeatability of the alignment. Hopefully, this new design will allow future group members to quickly and accurately measure the indistinguishability of a variety of interesting single photon sources.

The new design of the Hong-Ou-Mandel interferometer utilizes a fiber-coupled beamsplitter, and is inpired by the setup used in [13]. The design shown in Figure 6.1 would improve the stability of the interferometer, decouple the overlap at the beamsplitter from the interferometer alignment, and balance the coupling efficiencies of all four interferometer paths. Together, these improvements would allow us to run the measurement for a much longer time and increase the repeatability of the alignment, allowing us to gather more reliable statistics.

However, this design also introduces significant challenges not present in the free space Mach-Zender interferometer. Specifically, we must match the polarization basis (the orientation of horizontal and vertical polarizations) in free space to the basis within the

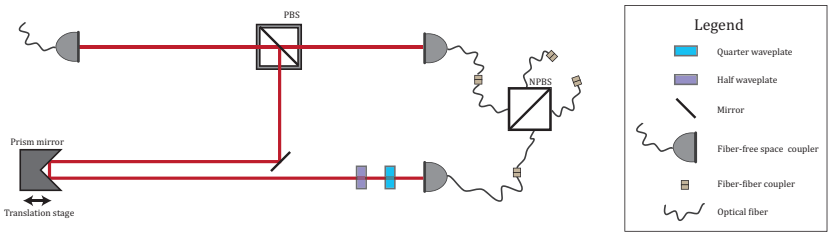


Figure 6.1: Design of a Hong-Ou-Mandel interferometer with fiber beamsplitter

polarization-maintaining (PM) fiber. This must be done precisely, otherwise the PM fiber will alter the polarization and the photons will not be reliably co- or cross-polarized when they arrive at the recombining beamsplitter. The design addresses this challenge by using a rotating mount for each fiber coupler that allows the PM fiber to be aligned to the free space polarization basis.

# References


[1] Altepeter, J. B., Jeffrey, E. R., & Kwiat, P. G. 2005. Phase-compensated ultra-bright source of entangled photons. *Optics Express*, **13**(22), 8951.

[2] Brańczyk, Agata M. 2017. *Hong-Ou-Mandel Interference*. Tech. rept.

[3] Cheung, J Y, Chunnilall, C J, Woolliams, E R, Fox, N P, Mountford, J R, Wang, J, & Thomas, P J. 2007. The quantum candela: a re-definition of the standard units for optical radiation. *Journal of Modern Optics*, **54**(3), 373–396.

[4] Erven, C., Meyer-Scott, E., Fisher, K., Lavoie, J., Higgins, B. L., Yan, Z., Pugh, C. J., Bourgoin, J.-P., Prevedel, R., Shalm, L. K., Richards, L., Gigov, N., Laflamme, R., Weihs, G., Jennewein, T., & Resch, K. J. 2014. Experimental three-photon quantum nonlocality under strict locality conditions. *Nature Photonics*, **8**(4), 292–296.

[5] Fox, Mark. 2006. *Quantum Optics, An Introduction*. Oxford: Oxford University Press.

[6] Giovannetti, Vittorio, Lloyd, Seth, & Maccone, Lorenzo. 2006. Quantum metrology. *Physical Review Letters*, **96**, 010401.

[7] Hamel, Deny R., Shalm, Lynden K., Hübel, Hannes, Miller, Aaron J., Marsili, Francesco, Verma, Varun B., Mirin, Richard P., Nam, Sae Woo, Resch, Kevin J., & Jennewein, Thomas. 2014. Direct generation of three-photon polarization entanglement. *Nature Photonics*, **8**(10), 801–807.

[8] Hanbury Brown, R., & Twiss, R. Q. 1956. A test of a new type of stellar interferometer on sirius. *Nature*, **178**(4541), 1046–1048.

[9] Hong, C K, Ou, Z Y, & Mandel, L. 1987. Measurement of subpicosecond time intervals between two photons by interference. *Physical Review Letters*, **59**, 2044–2046.

[10] Kwiat, Paul G., Mattle, Klaus, Weinfurter, Harald, Zeilinger, Anton, Sergienko, Alexander V., & Shih, Yanhua. 1995. New high-intensity source of polarization-entangled photon pairs. *Physical Review Letters*, **75**(24), 4337–4341.

[11] Martín-Martinez, Eduardo. 2018. *Notes for AMath 473, Advanced Quantum Theory.*

[12] Michelson, A. A., & Pease, F. G. 1920. Measurement of the diameter of Alpha-Orionis with the interferometer. *Astrophysical Journal*, **2**, 249–259.

[13] Reimer, M. E., Bulgarini, G., Fognini, A., Heeres, R. W., Witek, B. J., Versteegh, M. A. M., Rubino, A., Braun, T., Kamp, M., Höfling, S., Dalacu, D., Lapointe, J., Poole, P. J., & Zwiller, V. 2016. Overcoming power broadening of the quantum dot emission in a pure wurtzite nanowire. *Physical Review B*, **93**(19), 195316.

[14] Reimer, Michael E. 2009. *Electrostatic gating of deterministically positioned indium arsenide/indium phosphide quantum dots.* Ph.D. thesis, University of Ottawa.

[15] Santori, Charles M. 2003. *Generation of nonclassical light using semiconductor quantum dots.* Ph.D. thesis, Stanford University.

[16] Schlehahn, A., Thoma, A., Munnelly, P., Kamp, M., Höfling, S., Heindel, T., Schneider, C., & Reitzenstein, S. 2016. An electrically driven cavity-enhanced source of indistinguishable photons with 61% overall efficiency. *APL Photonics*, **1**(1), 011301.

[17] Thoma, A., Schnauber, P., Böhm, J., Gschrey, M., Schulze, J.-H., Strittmatter, A., Rodt, S., Heindel, T., & Reitzenstein, S. 2017. Two-photon interference from remote deterministic quantum dot microlenses. *Applied Physics Letters*, **110**(1), 011104.

# Appendix A

# Autocorrelation Function in the Fock Basis

In this appendix, we derive the dependence of the $g^{(2)}(0)$ function on the photon number state of the input field. We start from the expression for $g^{(2)}(\tau)$ introduced in equation 4.5, and relabel the fields at the output ports of the beamsplitter as $\hat{a}_3^\dagger$ and $\hat{a}_4^\dagger$, the input field as $\hat{a}_1^\dagger$, and the empty input port of the beamsplitter as $\hat{a}_2^\dagger$ (in a Hanbury Brown-Twiss experiment, the second input port is always in the vacuum state).

Under this new labeling scheme, the $g^{(2)}(\tau)$ function, in operator form, is:

$$g^{(2)}(\tau) = \frac{\left\langle\!\left\langle \hat{n}_3(t)\, \hat{n}_4(t+\tau) \right\rangle\!\right\rangle}{\left\langle\!\left\langle \hat{n}_3(t) \right\rangle\!\right\rangle \left\langle\!\left\langle \hat{n}_4(t+\tau) \right\rangle\!\right\rangle}, \tag{A.1}$$

where the double angle brackets signify both time averaging and a quantum expectation value:

$$\left\langle\!\left\langle \hat{f}(t) \right\rangle\!\right\rangle = \frac{1}{T} \int_T \left\langle \hat{f}(t) \right\rangle dt. \tag{A.2}$$

We are deriving the second-order autocorrelation formula only for time delay $\tau = 0$:

$$g^{(2)}(0) = \frac{\langle \hat{n}_3(t)\, \hat{n}_4(t) \rangle}{\langle \hat{n}_3(t) \rangle \langle \hat{n}_4(t) \rangle}; \tag{A.3}$$

we take the time average, as given in Equation A.2, and rewrite the number operators as creation and annihilation operators, to obtain:

$$g^{(2)}(0) = \frac{\langle \hat{a}_3^\dagger \hat{a}_3 \hat{a}_4^\dagger \hat{a}_4 \rangle}{\langle \hat{a}_3^\dagger \hat{a}_3 \rangle \langle \hat{a}_4^\dagger \hat{a}_4 \rangle}. \tag{A.4}$$

We can easily rewrite the numerator in normal order, because $[\hat{a}_3, \hat{a}_4^\dagger] = 0$:

$$g^{(2)}(0) = \frac{\langle \hat{a}_3^\dagger \hat{a}_4^\dagger \hat{a}_4 \hat{a}_3 \rangle}{\langle \hat{a}_3^\dagger \hat{a}_3 \rangle \langle \hat{a}_4^\dagger \hat{a}_4 \rangle} \tag{A.5}$$

Applying the same beamsplitter unitary as equations 5.1 and 5.2, with $p_r = p_t = 0.5$, to modes 3 and 4 yields the relationship:

$$\hat{a}_3^\dagger = \frac{1}{\sqrt{2}}\left(\hat{a}_1^\dagger + \hat{a}_2^\dagger\right), \tag{A.6}$$

$$\hat{a}_4^\dagger = \frac{1}{\sqrt{2}}\left(\hat{a}_1^\dagger - \hat{a}_2^\dagger\right). \tag{A.7}$$

We can now rewrite the autocorrelation function in terms of ladder operators on the input field. Keeping only the non-zero terms — there is only one term that does not interact with the vacuum state in field two, the empty input port of the beamsplitter — yields:

$$g^{(2)}(0) = \frac{\langle \hat{a}_1^\dagger \hat{a}_1^\dagger \hat{a}_1 \hat{a}_1 \rangle}{\langle \hat{n}_1 \rangle^2}. \tag{A.8}$$

Recognizing that there is only one non-vacuum input field, and thus we have no need to label the operators by mode, we define $\hat{n} = \hat{n}_1$ and obtain:

$$g^{(2)}(0) = \frac{\langle \hat{n}(\hat{n} - \hat{\mathbb{1}}) \rangle}{\langle \hat{n} \rangle^2}. \tag{A.9}$$

Let us now compute the expectation value of an arbitrary operator $\hat{O}$, in an arbitrary single mode quantum state $\hat{\rho}$:

$$\langle \hat{O} \rangle_{\hat{\rho}} = \mathrm{Tr}(\hat{\rho}\,\hat{O}) = \sum_m \langle m | \,\hat{\rho}\,\hat{O}\, | m \rangle \,; \tag{A.10}$$

for convenience, we have chosen $\{|m\rangle\}$ to be the Fock basis.

We can express a general quantum state in the Fock basis as $\hat{\rho} = \sum_{nn'} \rho_{nn'} \, |n\rangle \, \langle n'|$; when applied to equation A.10, this yields:

$$\langle \hat{O} \rangle_{\hat{\rho}} = \sum_{m,n,n'} \rho_{nn'} \, \langle m|n\rangle \, \langle n'| \, \hat{O} \, |m\rangle = \sum_{m,n,n'} \rho_{nn'} \, \langle n'| \, \hat{O} \, |m\rangle \, \langle m|n\rangle \,. \tag{A.11}$$

Recognizing the spectral decomposition of the identity, we can further simplify the expression:

$$\langle \hat{O} \rangle_{\hat{\rho}} = \sum_{n,n'} \rho_{nn'} \, \langle n'| \, \hat{O} \left( \sum_m |m\rangle \, \langle m| \right) |n\rangle = \sum_{n,n'} \rho_{nn'} \, \langle n'| \, \hat{O} \, |n\rangle \,. \tag{A.12}$$

Assuming that the operator $\hat{O}$ is diagonal in the Fock basis, we let $p_n = \rho_{nn'}$:

$$\langle \hat{O} \rangle_{\hat{\rho}} = \sum_n p_n \, \langle n| \, \hat{O} \, |n\rangle \,. \tag{A.13}$$

Since we know that the operators $\hat{n}$ and $\hat{n}^2$ are diagonal in the Fock basis, we write the second-order autocorrelation function of a general quantum state:

$$g^{(2)}(0) = \frac{\sum_n p_n \, n \, (n-1)}{\left( \sum_n p_n \, n \right)^2}. \tag{A.14}$$

A pure Fock state, $|n\rangle$, takes an even more simple form:

$$g^{(2)}(0) = \frac{n-1}{n}. \tag{A.15}$$